Supplementary Information

Optical Diagnostics.

The SOP diagnostic was setup such that plasma emission in the 550-800 nm optical band along the laser axis was streaked in time for 500 ns. The SOP data can be used to infer the velocity of the plasma flow from the foil. The emission from the laser-drive can be seen clearly at 0 ns in Figures 2a,b. At 210 ± 10 ns, there is strong plasma emission at the sphere, indicating that the plasma has traveled the 15 mm from the foil-target to the sphere, thus indicating a flow velocity of 70 ± 3 km/s. The SOP data shown in Figures 2a,b indicates the presence of transients between 200-300 ns. These transients are present in both the magnetized and non-magnetized cases and so are caused by the interaction of the plasma with the sphere, not by the magnetic field.

The Mach-Zender interferometry diagnostic was implemented using a 2ω Quantaray laser. The interferometry diagnostic had a ≈ 25 mm field-of-view, 250 ps gate time and looked perpendicularly to the laser axis (similarly to the view shown in Figure 1b). A reference image with no plasma present was taken before each laser-shot. The difference between the pre-shot image and on-shot image can then be used to infer the electron density. The electron density colour maps were generated using the Interferometric Data Evaluation Algorithm (IDEA) software. Lineouts of the electron density along the laser-axis for these two cases are shown in Figure S1 (see also Figures 2c,d). The electron density rises sharply close to the sphere in the magnetized case, but streams smoothly around the sphere in the non-magnetized case and so the electron density remains roughly constant. We notice, however, that shot-to-shot variations and noise in the interferometry data are $3\text{-}7 \times 10^{17}$ cm^{-3}, and so taking a bulk electron density 5×10^{17} cm^{-3} in the upstream flow is appropriate.

The optical spectroscopy diagnostic spectrally resolved the optical emission of the plasma on the laser axis, 12 mm from the target foil. The absolute spectral response of the diagnostic was made using a white light calibration, enabling the true spectrum to be recovered from the raw data. The optical spectrum was then fitted using the PrismSPECT software.

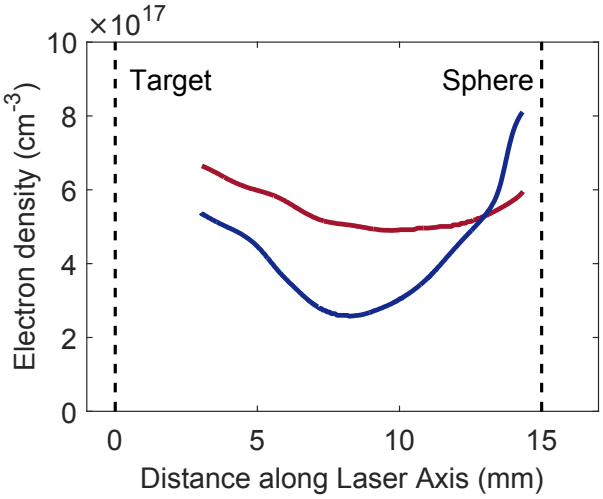

Figure 1: **Electron density profiles**. Electron density lineouts taken along the the laser-axis for the magnetized (blue) at 290 ns and non-magnetized (red) shot at 300 ns.

PrismSPECT Simulations: Optical Spectroscopy. The collisional-radiative code PrismSPECT [31] was used to fit the optical spectroscopy data. An electron density of 5×10^{17} cm^{-3} was used although the fits are broadly insensitive to electron density in the range 10^{17}-10^{18} cm^{-3}. From Figure 2g, it can be seen that temperatures of 2-4 eV fit the data whilst temperatures of 1 eV and 5 eV do not match the data. A bulk electron temperature of 3 +/- 1 eV best fits the data.

FLASH Radiation-Hydrodynamic Simulations 2-dimensional, radiation-magnetohydrodynamic simulations were performed using the publicly available code FLASH. FLASH is a parallel, multi-physics, adaptive-mesh-refinement (AMR), finite-volume Eulerian code. The simulations performed here include many of the high-energy density capabilities of the code [32], such as three-temperature MHD solvers, non-ideal MHD effects such as magnetic resistivity, heat exchange between ions and electrons, implicit thermal conduction and radiation transport in the multi-group diffusion approximation, and laser energy deposition via inverse Bremsstrahlung.

The FLASH simulations [32] were set up to fully reproduce the laser-plasma interaction and the resulting flow expansion and collision with the obstacle. We have performed simulations with and without a constant ambient

field of 5 kG strength orientated perpendicularly to the laser axis, which emulates the dipole field of the experiment within the region adjacent to the sphere. simulations were set up such that the computational domain (2 cm $\times$ 4 cm) was symmetric about the laser-axis and, utilizing FLASHs AMR, we were able to resolve spatial scales down to 8 μm. Spatial reconstruction was carried out using a 3rd-order piecewise parabolic method (PPM) [33] and a minmod limiter, while temporal integration was done with the second-order unsplit USM algorithm [34]. The upwind fluxes were computed using the Harten-Lax-van Leer Contact (HLLC) [35] Riemann solver. We carried out the simulations using the SCARF-MagnaCarta cluster at the Rutherford Appleton Laboratory and the Asterix cluster of the Flash Center for Computational Science at the University of Chicago.

The simulation predictions closely resemble what was observed in the experiment. The plasma outflow from the foil target travels at 70 km/s, reaching the sphere at $\sim$ 200 ns, as seen in the experimental data. In both the field and non-field cases, a shock forms at the sphere surface. Similarly to the experiment, the non-field case results in a much thinner bow-like shock than the field case. As shown in Figure 2 of the paper, the simulation predicts bulk electron densities $\sim 5 \times 10^{17}$ cm^{-3}, rising to over 10^{18} cm^{-3} at the shock front, in agreement with the laboratory data. Additionally, at the time and spatial position that the optical spectroscopy data was taken, FLASH predicts an electron temperature of 3 eV, matching the experiment. The quantitative agreement between simulation and experiment gives us confidence in the accuracy of the electron temperature predictions from the FLASH code. The electron temperature is $\sim$ 200 eV at the beginning of the laser drive, but then it adiabatically cools to a bulk electron temperature $\sim$ 3 eV for times $t > 50$ ns.

Electric Field Calculation The FLASH simulations can be used to gain insight into the nature of the shock formation. Although the FLASH simulations did not include the dipole magnetic field of the obstacle, the constant field used in the simulations can give an indication of the strength of the electric field produced at the shock.

The electric field influencing the plasma near the sphere can be estimated using [22] $E_\parallel \sim \frac{1}{2\mu_0 n_i e}\frac{dB_\perp^2}{dx}$, where $E_\parallel$ is the electric field parallel to the flow axis, n_i is the ion density and $B_\perp$ is the magnetic field perpendicular to the flow axis and the derivative is taken along the flow axis direction.

X-ray Spectrometer Setup

The X-ray spectrometer consisted of a 25×50 mm^2 RbAP crystal, with 100 mm radius of curvature, operating at a Bragg angle of 43.5^o and is cylindrically bent along the long axis of the crystal. In this Von-Hamos geometry, the X-rays from the plasma are focused onto a 60×100 mm^2 image plate detector as shown in Figure S1. This setup allows for both spectral resolution (620–770 eV full range) and spatial discrimination with 1:1 magnification [36]. By geometrical considerations [36], it is possible to show that a 1 mm source size is blurred on the image plane by 20 μm. Both the crystal and image plate were housed in a light-tight enclosure containing a small window through which the X-rays from the sample could reach the crystal (see Figure S1). The window was filtered with 5 μm of Aluminium.

The raw signal on the image plate was analysed in the following manner. First, the background noise across each data set was removed. The background signal varies linearly along both the horizontal and vertical axes of the image plate. This background can be readily subtracted from the data signal. To calibrate the energy scale along the image plate, both PVDF and CH foils, placed at the focal position of the spectrometer, were used as shown in Figure S1. The PVDF foil produces a fluorine line at 731 eV (similarly to the main experiment). The CH foil (as expected) does not produce a line at 731 eV. Traces of Oxygen present in the vacuum chamber (rather than in the material content of the target) produce lines at 653 eV, 664 eV and 698 eV that can be seen on the image plate.

The background corrected data showed a clear line at 731 eV for all shots, the Fluorine He-α line. For every shot, the signal from the Fluorine He-α line at a given distance from the sphere has been frequency-integrated and averaged over a 0.3 mm interval. To collate the results, data from shots with the same type of sphere were averaged together. To aid comparison, different data sets are rescaled such that the peak of the spectrally resolved emission in the region close to the sphere (as shown in Figure 3) for the magnetized case is set to unity.

The standard deviation of the signal within the 0.3 mm spatial band determines the primary error for each data point as shown in Figure 3. Additionally, since the final data points are an average of several shots, the overall error is the sum in quadrature of the error for individual shots.

OSIRIS PIC Simulations. In these OSIRIS [37] PIC simulations, a hydrogen plasma is injected continuously from the left hand boundary with temperature $T_e = T_i \simeq 3$ eV and velocity v_0. Due to the high computational costs, OSIRIS simulations were performed with a flow velocity $\frac{v_0}{c} = 0.1$ and an electron-ion mass ratio of $\frac{m_i}{m_e} = 100$, where m_i is the average ion mass and m_e is the electron mass. As discussed in the main text, the simulation results need to be scaled back to laboratory conditions. We have also assumed there is an externally applied magnetic field $\mathbf{B} = \mathbf{B}_0 + \mathbf{B}_\mathrm{d}$, where $\mathbf{B}_\mathrm{d}$ is the sphere dipolar field (modeled in the simulation plane) and $\mathbf{B}_0$ is an upstream magnetic field with a magnitude chosen such that the ion Larmor radius is $\rho_i \simeq 8c/\omega_{pi}$ (where ω_{pi} is the ion plasma frequency), similarly to experimental conditions at the shock position. simulation domain has dimensions

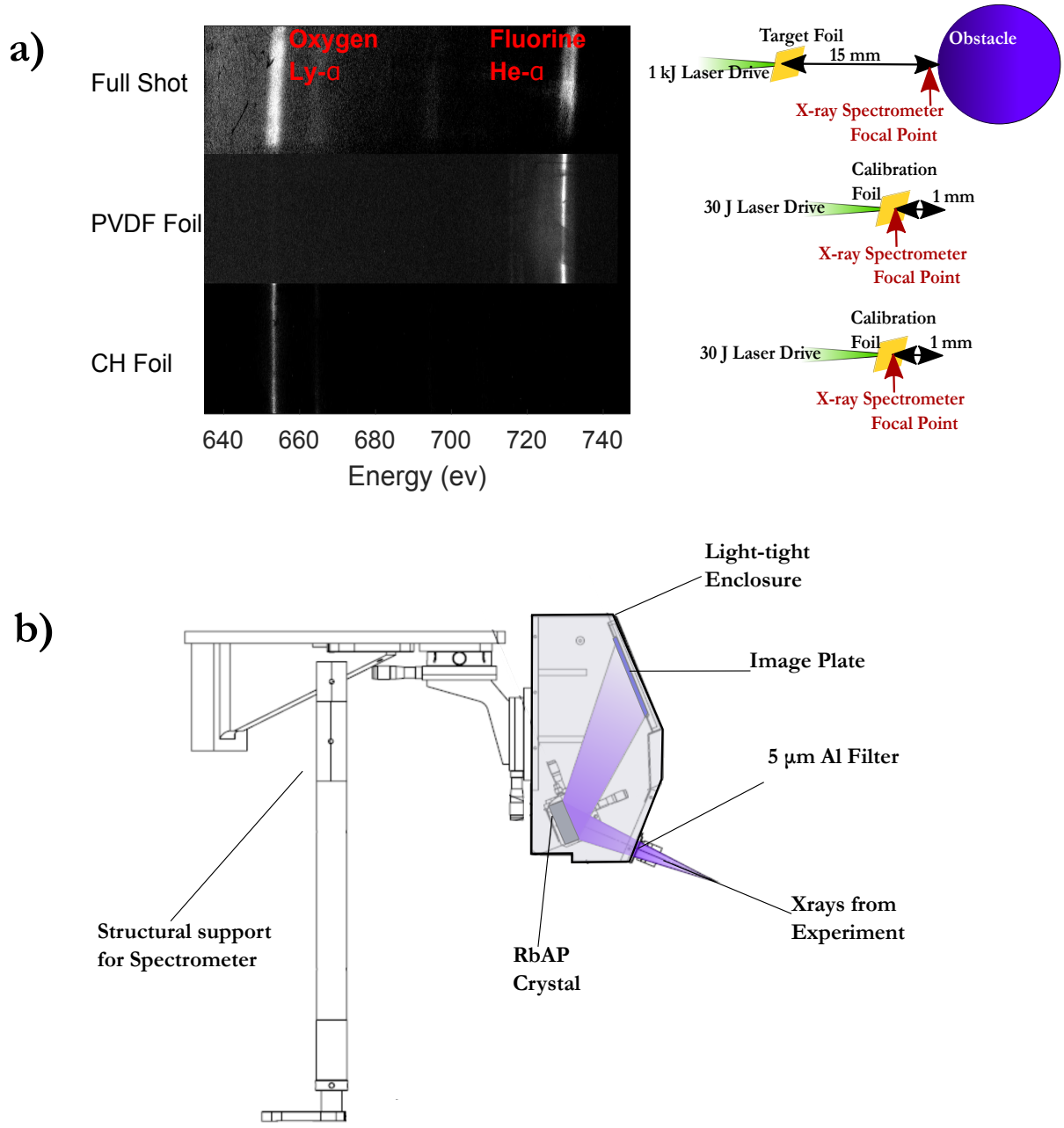

Figure 2: **X-ray Spectrometer setup and Calibration**. a) Spectra from PVDF and CH foil shots and a full shot. The foil shots can be used for calibrating the energy of the X-rays. Experimental setup for the PVDF and CH calibration foil shots. The foil is positioned at the focal point of the X-ray spectrometer, 1 mm from the sphere position. For these shots, no sphere is present. b) Schematic of X-ray spectrometer, including how the crystal is housed.

$L_x \times L_y = 960 \times 1600 c/\omega_{pe}$ and the grid resolution is 10 cells per c/ω_{pe} in both directions, with 25 simulation particles per cell per species. Periodic boundary conditions are used in the y direction, and open boundary conditions are used for the right hand boundary. Figures 4 a) and b) show only a fraction of the simulation domain.

The plasma ions are reflected at the shock front and travel upstream to a distance of the order of the ion Larmor radius. The electron temperature was extracted from the OSIRIS simulations by mapping the electron distribution function in space and computing its second central moment. The downstream temperature was found to be 10–100 keV and is maximum at the bow shock flanks.

The convergence of OSIRIS simulations with scaled up/down plasma velocities/ion-electron mass ratios has

been confirmed by comparing the results of previous simulations similar to the one presented here with plasma fluid velocities down to 0.02c and ion-electron mass ratios up to $m_i/m_e = 900$ (see [23]). These parameters, in particular the ion-electron mass ratio, control the separation between ion and electron temporal and spatial scales. Scaling them appropriately allows a significant reduction of the computational effort to perform the numerical experiments, yet we are still able to gain important physical insight into the dynamics of these complex systems.

A more accurate description of the experiment could be obtained by using, for example, a multi-species plasma. In particular, the interaction between the different species with the field at different times is expected to lead to a transient. However, the transient always happens when the plasma cavity is formed and before the turbulent region is excited (which happens on ∼1 ion gyroperiods, in the collisionless limit). Whether this transient time can be extended with the introduction of a multi species plasma is an interesting question, but one very difficult to answer with full PIC simulations. This would require separating clearly the time scales of the different ion species, which is computationally extremely demanding.

Despite the OSIRIS simulations being collisionless and the laboratory plasma being mildly thermally collisional, the OSIRIS results can still be applied to the laboratory plasma. The electron-electron collisions in the laboratory plasma preserve the electron isotropy and so the temperature anisotropy as seen in the OSIRIS simulations will be less pronounced in the laboratory plasma. The electron-electron collisions do not inhibit the development of the modified two-stream instability (see Plasma Collisionality below) and so the average hot electron energy in the OSIRIS simulations (50 keV) can still be scaled to laboratory conditions to give a reasonable estimate of the average hot electron energy in the laboratory (45 eV), see Equation 2.

Average electron energy Calculation. First the average energy gain of the electrons accelerated by lower-hybrid turbulence [9] is estimated. Assuming that the energy is transferred from the ions to the electrons with an efficiency factor α, energy flow balance requires that

$$\alpha n_i m_i u^3 = n_e E_e \sqrt{\frac{E_e}{m_e}}, \tag{1}$$

where n_i and n_e are the ion and electron densities of the resonant particles, u is the ion velocity, and E_e is the resonant electron energy. The resonant electron density can be obtained by balancing the growth rate of the ion instability against Landau damping due to electrons moving parallel to the magnetic field, hence

$$n_e = E_e \frac{n_i}{m_i u^2}. \tag{2}$$

Equations 1 and 2 can then be combined to give Equation 1.

PrismSPECT Simulations: X-ray Spectroscopy. PrismSPECT was used to calculate the X-ray emission from the predicted energetic electron population of lower-hybrid accelerated electrons. The PrismSPECT calculation uses a bulk plasma electron density of 5×10^{17} cm^{-3} and electron temperature of 3 eV, for a range of efficiency factors α from 0–0.5. For a given α, the energetic electron population had a Maxwellian distribution with average energy given by Equation 1 and density given by Equation 2.

Plasma collisionality.

Since the thermal background is relatively cold compared with the velocity of the reflected ions, the reflected ions will be dragged by the electrons in the thermal plasma and so the ion-electron collision mean-free-path (note not the thermal collision mean-free-path) is the most important quantity in determining whether or not the modified two-stream instability will be damped by collisions. Using PrismSPECT, a downstream plasma electron density of 10^{17} cm^{-3} and 3 eV electron temperature, the ionisation of the Carbon, Hydrogen and Fluorine ions is 3, 1 and 2 respectively. The ion-electron collision distance for the electrons to slow down the beam of reflected ions can be calculated using standard expressions. We note that for our case, the thermal energy of the electrons is large compared to the reflected ion beam energy.

For the three different ions, this calculation gives a distance for the ions to be slowed down by electron collisions as 1, 1.5 and 5 mm for the Hydrogen, Carbon and Fluorine ions respectively. This means that for a 3 eV background plasma, the Hydrogen and Carbon reflected ions will be slowed down within ∼ 1 mm, whereas the Fluorine ions are effectively collisionless on the scales of interest for electron heating. Electron-electron collisions on the other-hand are the dominant mechanism for electron scattering. Although the electrons are only weakly magnetized ($\omega_g \tau_e \lesssim 1$), they can be accurately treated as an isotropic fluid, and as such, can be shown to satisfy the usual fluid limit of the lower-hybrid instability [17]. The ∼ 30 eV electrons, inferred from PrismSPECT simulations, on the other hand will be magnetised in the strong pre-shock fields. However, their gyro-radii are still not sufficient to permit collisionless transport across the shock [38].

References

[1] K. Koyama et al. *Evidence for shock acceleration of high-energy electrons in the supernova remnant SN1006*, Nature 378, 255-258, 1995

[2] A. Masters et al. *Electron acceleration to relativistic energies at a strong quasi-parallel shock wave*, Nature Physics 9, 164-167, 2013

[3] E. A. Helder et al. *Observational Signatures of Particle Acceleration in Supernova Remnants*, Space Science Reviews 173, 369-431, 2012

[4] R. Blandford and D. Eichler *Particle acceleration at astrophysical shocks: A theory of cosmic ray origin*, Physics Reports 154, 1, 1987

[5] R. Van Weeren et al. *Particle Acceleration on Megaparsec Scales in a Merging Galaxy Cluster*, Science 330, 347-349, 2010.

[6] A. Marcowith et al. *The microphysics of collisionless shock waves*, Reports on Progress in Physics 79, 046901, 2016

[7] T. Amano and M. Hoshino *Electron Injection at High Mach Number Quasi?−perpendicular Shocks: Surfing and Drift Acceleration*, The Astrophysical Journal 661, 190-202, 2007

[8] M. Riquelme and A. Spitkovsky *Electron injection by Whistler waves in non-relativistic shocks*, The Astrophysical Journal 733, 63, 2011

[9] R. Bingham et al. *Generation of X-rays from Comet C/Hyakutake 1996 B2*, Science 275, 49–51, 1997

[10] K. G. McClements et al. *Acceleration of cosmic ray electrons by ion-excited waves at quasiperpendicular shocks*, Monthly Notices of the Royal Astronomical Society 291, 241–249, 1997

[11] R. Bingham et al. *X-ray emission from comets, cometary knots and supernova remnants*, The Astrophysical Journal 127, 233-237, 2000

[12] J. Vink and M. J. Laming *On the Magnetic Fields and Particle Acceleration in Cassiopeia A*, The Astrophysical Journal 584, 758-769, 2003

[13] N. J. Fisch. *Theory of Current Drive in Plasmas*, Reviews of Modern Physics, Volume 59, 175-, 1987

[14] M. Porkolab et al. *High-Power Electron Landau-Heating Experiments in the Lower Hybrid Frequency Range in a Tokamak Plasma*, Physical Review Letters, 53, 1229, 1984

[15] R. Cesario et al. *Current drive at plasma densities required for thermonuclear reactors*, Nature Comms. 1 (5), 55, 2010

[16] J. A. Eilek and J. C. Weatherall in *Diffuse thermal and relativistic plasma in galaxy clusters*. Edited by Hans Bohringer, Luigina Feretti, Peter Schuecker. Garching, Germany: Max-Planck-Institut fur Extraterrestrische Physik, p. 249, 1999

[17] J. B. McBride et. al. *Theory and Simulation of Turbulent heating by the Modified Two-Stream Instability*, Physics of Fluids 15, 2367, 1972

[18] I. H. Cairns and G. P. Zank *Turn-on of 2-3 kHz radiation beyond the heliopause*, Geophysical Research Letter 29, 1143, 2002

[19] Y. P. Zakharov et al. *Simulation of astrophysical plasma dynamics in the laser experiments*, AIP Conference Proceedings 369, 357-362, 2008

[20] P. Beiersdorfer et al. *Laboratory Simulation of Charge Exchange-Produced X-ray Emission from Comets*, Science 300, 1558–1559, 2003

[21] A. R. Bell et al. *Collisionless shock in a laser-produced ablating plasma*, Physical Review A 38, 1363, 1988

[22] R. Z. Sagdeev, *Cooperative phenomena and shock waves in collisionless plasmas*, Reviews of plasma physics 4, 23, 1966

[23] F. Cruz et al. *Formation of collisionless shocks in magnetized plasma interaction with kinetic-scale obstacles*, Physics of Plasmas 24, 022901, 2017

[24] Y. Omelchenko et al. *Numerical simulation of quasilinear relaxation of an ion ring and production of superthermal electrons* Soviet Journal Plasma Phys. 15 (6) June 1989

[25] M. J. Laming *Accelerated electrons in Cassiopeia A: thermal and electromagnetic effects*, The Astrophysical Journal 563, 828, 2001

[26] T. Yamamoto et al. *Experimental Observation of the rf-Driven Current by the Lower-Hybrid Wave in a Tokamak*, Physical Review letters 45, 716, 1980

[27] R. L. Stenzel et al. *Electrostatic waves near the lower hybrid frequency*, Physical Review A 11, 2057, 1975

[28] R. W. Boswell et al. *Very efficient plasma generation by whistler waves near the lower hybrid frequency*, Plasma Physics and Controlled Fusion 26, 10, 1984

[29] M. Torney et al. *Modelling X-ray Line and Continuum Emission from Comets*, Physica Scripta, 2002, T98

[30] T. E. Cravens et al. *Comet Hyakutake x-ray source: Charge transfer of Solar wind heavy ions*, Geophysical Research Letters 24, 1, 1997

[31] J. J. MacFarlane et al. *SPECT3D - A multi-dimensional collisional-radiative code for generating diagnostic signatures based on hydrodynamics and PIC simulation output*, High Energy Density Physics 3, 181-190, 2007

[32] P. Tzeferacos et al. *FLASH MHD simulations of experiments that study shock-generated magnetic fields*, High Energy Density Physics 17, 24-31, 2015

[33] P. Colella et al. *The piecewise parabolic method (PPM) for gas-dynamical simulations*, Journal of Computational Physics 54, 174 (1984)

[34] D. Lee *An implicit ghost-cell immersed boundary method for simulations of moving body problems with control of spurious force oscillations*, Journal of Computational Physics 243, 269 (2013)

[35] S. Li *An HLLC Riemann solver for magneto-hydrodynamics*, Journal of Computational Physics 203, 344 (2005)

[36] A. P. Shevelko *X-Ray Spectroscopy of laser-produced plasmas using a von Hamos spectrograph*, Proc. SPIE 3406, 91, 1998

[37] R. A. Fonseca et al. *OSIRIS: A Three-Dimensional, Fully Relativistic Particle in Cell Code for Modeling Plasma Based Accelerators*, Lecture Notes in Computer Science 2331, 342-351 (Springer, 2002)

[38] G. Gregori et al. *The generation and amplification of intergalactic magnetic fields in analogue laboratory experiments with high power lasers*, Physics Reports 601, 1–34, 2015